Caustic Interpretation of the Abruptly Autofocusing Vortex beams

NA XIAO,[1] CHEN XIE,[1,*] ERSE JIA,[1] JIAYING LI,[1] REMO GIUST,[2] FRANÇOIS COURVOISIER,[2] AND MINGLIE HU[1]

[1]*Ultrafast Laser Laboratory, Key Laboratory of Opto-electronic Information Science and Technology of Ministry of Education, College of Precision Instruments and Opto-electronics Engineering, Tianjin University, 300072 Tianjin, China*
[2] *FEMTO-ST,Université de Bourgogne-Franche-Comté UMR-6174, 25030 Besancon, France*
*xie_chen@tju.edu.cn

Abstract: We propose an effective scheme to interpret the abruptly autofocusing vortex beam. In our scheme, a set of analytical formulae are deduced to well predict not only the global caustic, *before and after the focal plane*, but also the focusing properties of the abruptly autofocusing vortex beam, including the axial position as well as the diameter of focal ring. Our analytical results are in excellent agreement with both numerical simulation and experimental results. Besides, we apply our analytical technique to the fine manipulation of the focusing properties with a scaling factor. This set of methods would be beneficial to a broad range of applications such as particle trapping and micromachining.

1. Introduction

With the use of radially symmetric Airy beams, abruptly autofocusing (AAF) beams were first introduced theoretically in 2010 [1] and were demonstrated experimentally in 2011 [2]. Different from the focusing effects mediated by lenses or Kerr nonlinearities, AAF beams can maintain a bottle-like beam with zero intensity on the optical axis and abruptly concentrate the field intensity at a focal point by the optical field structure itself. AAF beams are commonly produced either in the Fourier space with a cubic phase term [2,3], or in the direct space with sublinear chirp phase [4] or 3/2 order radial phase [5]. Efficient methods are also proposed to generate AAF beams with arbitrary caustics [6-9]. Due to the notable autofocusing property, AAF beams have attracted intense interests and spawned numerous applications like optical trapping and particle micromanipulation [10-13], material processing [14] and generation of light bullets [15]. Besides AAF beams, other beams with autofocusing properties have also been found and explored [16-19]. On the other hand, the optical vortices are structured light fields with helical phase fronts described as exp ($il\theta$), where l is so-called topological charge and θ is the azimuthal angle [20]. Optical vortex beams have acquired considerable interest due to their intriguing features such as the doughnut-shaped spatial profile and the phase singularity. With these interesting characteristics, optical vortex beams are useful in quantum information [21], optical communication [22,23], particle micromanipulation [24,25] and material processing [26,27].

In the last decade, by encoding the phase of optical vortices with the AAF beams on the spatial light modulator (SLM), abruptly autofocusing vortex (AAFV) beams are generated. The influence of the optical vortices on the intensity distribution of the AAF beams during

propagating are also investigated [28-37]. For AAF beams with vortices, AAFV with central hollow regions are generated and the autofocusing property can be enhanced with optical vortices, especially with a large topological charge or a negative launch angle [28-30]. Compared with the conventional AAF beams, there are some tiny changes of the axial positions as well as the diameters of the focal rings [31-33]. However, the tiny changes mentioned above were simply detected and measured, without any clear explanations. Besides, the theoretical descriptions of the global caustic of AAFV beams are also missing in the literature. The presence of a vortex severely modifies the trajectory of the intensity maximum[38,39]. This is particularly true in the focal region, but is also apparent earlier in the propagation.

In this paper, we focus on the generation of AAFV beams in the direct space and interpret the AAFV beams based on a set of ray-based caustics schemes [40-44]. First, we deduce a set of analytical formulae to describe the caustics *before and after* the focus of the AAFV beam. Meanwhile, the axial position and the diameter of the focal ring can also be obtained using our formulae. Furthermore, with a scaling factor *s*, the axial positions and the diameters of the focal rings can be accordingly manipulated, which have great convenience for the applications of AAFV beams. Our analytical results are in excellent agreements with the experimental and numerical results.

2. Phase mask design and Experimental setup

In this work, we used the AAF beams generated in the direct space based on our previous work [9]. This AAF beams can be synthesized from the symmetrically self-accelerating beams along polynomial curves, *i.e.* $r = r_0 - az^n$, where r is the radial coordinate, r_0 is the radius of the initial central disk and a is the shape factor of the accelerating trajectory. After combining the vortex phase, the total phase of the AAFV beams can read as:

$$\phi(r,\theta) = \phi_{AAF} + \phi_{vortex} = -k \frac{n^2}{(2n-1)(n-1)} \left[(n-1)a\right]^{\frac{1}{n}} (r-r_0)^{\frac{2n-1}{n}} + l\theta \quad (1)$$

where k is the wave number defined as $k = 2\pi/\lambda$ and λ is the laser wavelength.

The above AAFV beams can be generated in the direct space by encoding the above phase on the SLM in our experimental setup (schematically shown in Fig. 1). The collimated Gaussian beam, delivered from a home-made ultrafast fiber laser centered at 1065nm, is first expanded to 8 mm with a telescope consisting of the lens f = 35 mm and the lens f = 125 mm. Then, the expanded beam is incident upon a phase-only SLM (Holoeye SLM-Pluto, 1920x1080 pixels). With the phase mask imposed, the reflected light becomes AAFV beam and is de-magnified after a 4f system (lens L_1, focal length f = 1 m, microscope objective MO_1, x50). An iris is installed close to MO_1 to block the undesired orders and just retain the first order of diffraction light. Another set of the microscope objective (MO_2, x50), the lens L_2 (f = 500 mm) and the CCD camera together make up the imaging system. With the objective MO_2 installed on the motorized translation stage, the intensity profiles at each z position along beam propagation would be scanned and synthesized into a 3D profile.
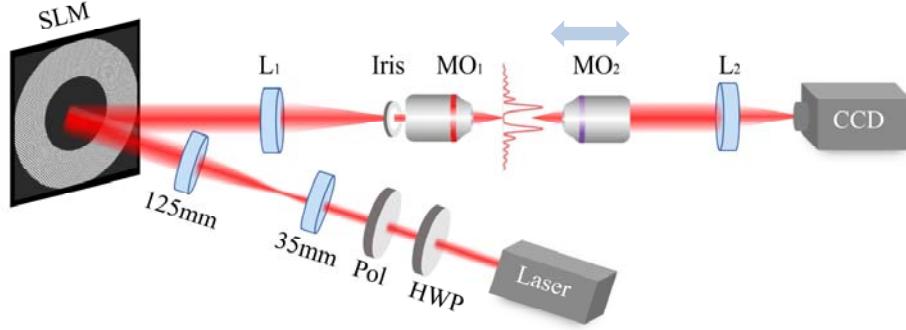
Fig. 1. Schematic of the experiment system. HWP: half-wave plate; Pol: polarizer; SLM: spatial light modulator; L: lenses; MO1 and MO2: microscope objectives. The analytical formulae of the global caustic and focusing properties of AAFV beams

Up to now, the previous works on AAFV beams focus on the autofocusing behaviors and numerical simulations are implemented to investigate this topic. However, only one half of the trajectory is approximated by the corresponding self-accelerating curves before the focal ring. The analytical trajectory of the whole beam is still absent. In this section, we deduce a set of analytical formulae to describe the global caustic of AAFV beam with the ray-based methods. With the help of our analytical results, the parameters of the focal ring including the axial position as well as the focal ring size can also be obtained.

In view of the scalar and linear propagation in air, the direction of our AAFV beam can be obtained from the gradient of its phase (*i.e.* $\mathbf{k} \equiv \nabla \phi$) [45]. We rewrite the phase gradient along r as follows,

$$\frac{\partial \phi}{\partial r} = -k \frac{n}{n-1} \left[(n-1)a \right]^{\frac{1}{n}} \left(r - r_0 \right)^{\frac{n-1}{n}} \equiv -k \sin \gamma (r)$$

$$\sin \gamma (r) \equiv n a^{\frac{1}{n}} \left(\frac{r - r_0}{n-1} \right)^{\frac{n-1}{n}}$$

(2)

Thus, the unit vector of the ray at any location is shown in the cylindrical coordinate as follows,

$$\begin{bmatrix} u_r \\ u_\theta \\ u_z \end{bmatrix} = \begin{bmatrix} -\sin \gamma (r) \\ l / k \cdot r \\ \sqrt{1 - \sin^2 \gamma (r) - l^2 / k^2 r^2} \end{bmatrix}$$

(3)

Actually, this unit vector has the same form as that of the Bessel vortex beam in our previous work [45] except for a radially - dependent conical angle γ. Similarly, we can further obtain the parametric trajectory of any single ray emerging from the point $M_0 = (r,0,0)$ in the plane $z = 0$ to a running point M located in the z-plane. After simplification of the parametric equations [45], we found that the families of straight ray bundles emerging from the ring with the given radius r in the plane $z = 0$ lie on the hyperboloids [as shown in Fig. 2(a)], defined by:

$$\frac{\rho^2}{R^2(r)} - \frac{[z - z_w(r)]^2}{L^2(r)} = 1 \qquad \rho^2 = x^2 + y^2$$

$$R(r) = l \Big/ \sqrt{k^2 \sin^2 \gamma(r) + \frac{l^2}{r^2}}$$

$$L(r) = R(r) \sqrt{\frac{1 - \sin^2 \gamma(r) - l^2 / k^2 r^2}{\sin^2 \gamma(r) + \dfrac{l^2}{k^2 r^2}}} \tag{4}$$

$$z_w(r) = r \sin \gamma(r) \frac{\sqrt{1 - \sin^2 \gamma(r) - l^2 / k^2 r^2}}{\sin^2 \gamma(r) + \dfrac{l^2}{k^2 r^2}}$$

where $R(r)$, $L(r)$ and $z_w(r)$ are all related to r, n, and l. Taking the case with $n = 2$ and $l = 3$ as an example, the families of straight rays with two different given r are winding on two different hyperboloids as shown in Fig. 2(a), where only half of each x-z cut of these two hyperboloids are presented. Besides, the projections of the intersections between the hyperboloids and the x-z plane ($y = 0$) are also shown in the plane $y = -20$ μm. As the Eq. (4) represents a family of hyperboloids depending on the initial ring radius r in the plane $z = 0$, different hyperboloids are overlapped with the finite and variable parameter r. For simplicity, the intersections between different hyperboloids and the horizontal plane $y = 0$ are plotted with gray solid curves in Fig. 2(b).
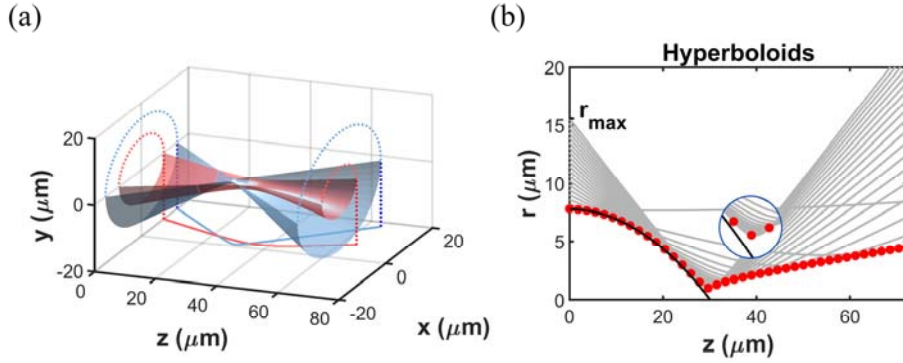

Fig. 2. Geometrical description of the beam with a given set of the degree of the polynomial n=2 and the topological charge l=3: (a) The x-z cut of two different hyperboloids formed by the corresponding family of rays emerging from the ring in the plane z=0 with specific radii r_1=11 μm and r_2=9 μm (blue and red surfaces); and the corresponding intersections (blue and red solid curves) projected in the plane of y=-20 μm; (b) The global caustic of the AAFV beams (red dots) solved from the Eq. (7) together with the intersections between the hyperboloids and the y=0 plane (gray solid curves), the trajectory of the corresponding AAF beam (black solid curve). The inset shows a larger version of the focus position.

In order to interpret the global structure of the AAFV beam, it is important to find the global caustic. In geometrical optics, the envelope of a family of curves or surfaces composed by a family of rays is defined as their caustic [42]. Therefore, the corresponding caustic of the AAFV beam is the envelope of the hyperboloids. For convenience, we rewrite Eq. (4) to define the hyperboloids as

$$F(r,\rho,z) = \frac{\rho^2}{R^2(r)} - \frac{[z - z_w(r)]^2}{L^2(r)} - 1 \tag{5}$$

Actually, the envelope of the family of surfaces, *i.e.* the global caustic, is formed by a set of *characteristic points* (which is tangent to each hyperboloids). These points are simply the solutions to the following equations [46].

$$F(r,\rho,z) = 0 \quad and \quad \frac{\partial F}{\partial r}(r,\rho,z) = 0 \tag{6}$$

After some algebra, we find the *characteristic points* composing the caustic can be analytically expressed as

$$z_1 = z_w - \frac{B}{2A} + \frac{\Delta}{2A}$$
$$z_2 = z_w - \frac{B}{2A} - \frac{\Delta}{2A} \tag{7}$$

where A, B, C and Δ are defined as

$$A = \frac{1}{L^2(r)}\left[\frac{L'(r)}{L(r)} - \frac{R'(r)}{R(r)}\right]$$

$$B = \frac{z_w'(r)}{L^2(r)} \tag{8}$$

$$C = -\frac{R'(r)}{R(r)}$$

$$\Delta \equiv \sqrt{B^2 - 4AC}$$

and the prime means the derivatives with respect to r.

The global caustic is composed of the ensemble of characteristic points $(\rho(z_1), z_1)$ and/or $(\rho(z_2), z_2)$ where z_1 and/or z_2 are positive. (We note that A is negative for most of the parameter range. When this is verified, z_1 and z_2 are both positive leaving the corresponding characteristic points located on each side of the focus). Therefore, the whole global caustic can be calculated from Eq. (4), Eq. (7) and Eq. (8). Taking the case with *n*=2 and *l*=3 as an example, the projection of the caustic trajectory in the *x-z* plane is plotted with the red dots in Fig. 2(b). In comparison, the polynomial trajectory of the corresponding AAF beam without vortices is also plotted with the black curve in Fig. 2(b). The inset of Fig. 2(b) shows a zoom-in window around the focal position. It is obvious that the caustics of these two AAF beams with and without vortices are almost indistinguishable until the focal region around *z*=30 μm, which is also mentioned in ref [28]. As the topological charge *l* increases, the discrepancies between these caustics also increase.

It is shown in references [4,9] that the wave amplitude around the focus of the AAF beam is determined mainly by the constructive interference of the continuum of ray emerging from the outmost circle in the initial plane (*z* = 0). In our case, the distance between the outmost circle and the optical axis (*i.e.* r_{max}=15.6 μm) would define the axial focal position of the AAFV beams as $z_l(r_{max})$ in the Eq. (7). Therefore, the focal ring diameter $2\times \rho(z_l)$ can be acquired from Eq. (4). This definition will be used in the following discussion on the focusing properties.

3. Results and discussions

3.1 The caustics and the focusing properties of AAFV beams

Based on the angular spectrum method [47], we numerically simulate the AAFV beams with the parameters corresponding to the setup in Fig. 1. As an example, we generate AAFV beams with the topological charge (l=2) and different degrees of polynomials (n=2, 3, 4) using the phase mask in Eq. (1). The other parameters are selected to fit our setup, *i.e.* $r_0=r_{max}/n$ and $a = 0.4\times10^{-3}$ m^{-1} , 0.9×10^{-4} m^{-2} and 0.3×10^{-4} m^{-3} for n=2, 3, 4 respectively. The numerical simulations and experimental results are shown in Fig. 3, where the measured 2D intensity profiles are extracted from the 3D data acquired with our setup. It is evident that our analytical caustics are in excellent agreement with the numerical simulation and experimental results. Importantly, we note that In a given case of n =4, the predefined polynomial (red dashed lines) predicts the beam path only up to the focus, , as shown as an example in Fig. 3(c) (red dashed line), while our deduced trajectory (white dash dot lines in Fig.3) distinctly describe the global caustic. addition, the presence of the vortex modifies the actual trajectory with respect to the polynomial path. This is particularly clear for AAFV beams with large topological charge (l = 5) such as in Fig. 4. In the case of n = 4 and l = 5, the ring expands significantly at the beginning of the propagation and then shrinks until the focal ring followed by an expanded open ring again [shown in Fig. 4(c)], which deviates from the monotonous trajectory of the predefined polynomial, *i.e.* $r = r_0 - az^n$. This behaviour can be understood because the distance of the lobe from the trajectory depends on the vortex order and on the local radius of curvature. The analytical caustics based on our theory accurately describe this behaviour.
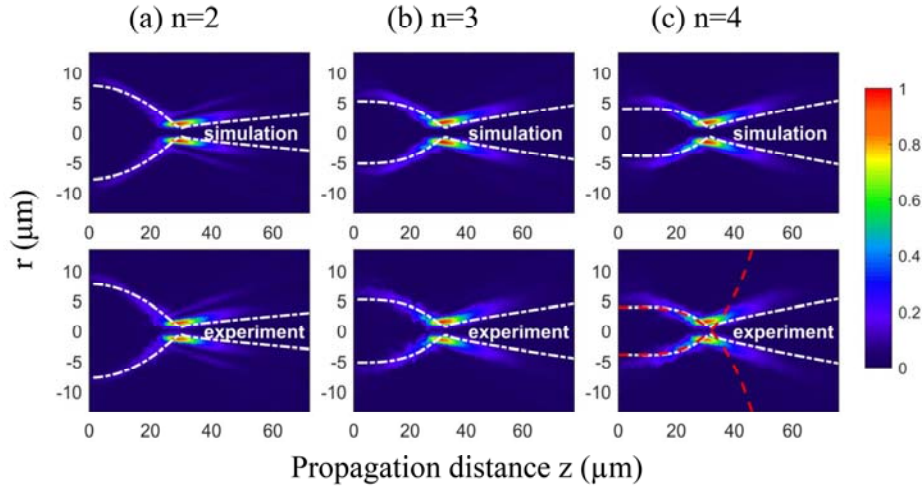

Fig. 3. The numerical simulation results and experimental results for AAFV beams of the same topological charge l=2 with different degrees of polynomials. (a) n=2, (b) n=3, (c) n=4. The analytical caustics are plotted in white dash dot lines, and the predefined polynomial trajectory (rad dashed lines) for n=4 is superimposed for comparison.
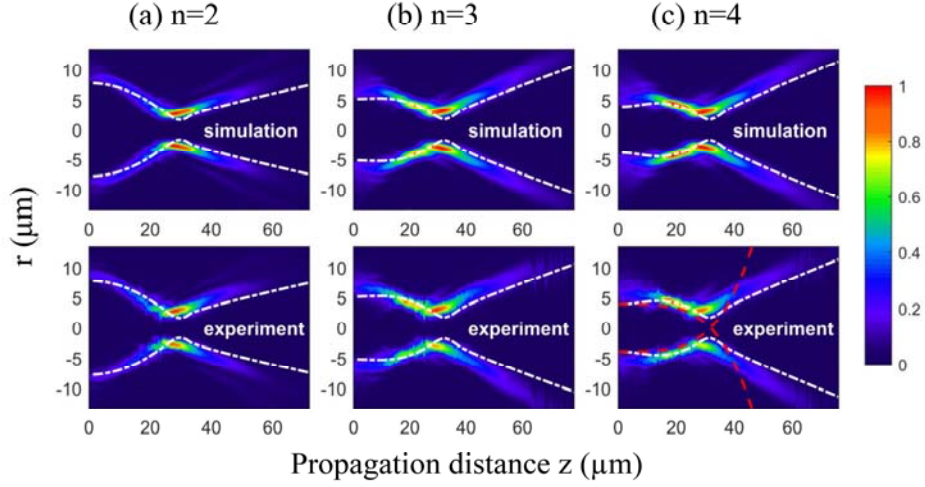
Fig. 4. The numerical simulation results and experimental results for AAFV beams of the same topological charge *l*=5 with different degrees of polynomials. (a) *n*=2, (b) *n*=3, (c) *n*=4. The analytical caustics are plotted in white dash dot lines, and the predefined polynomial trajectory (rad dashed lines) for n=4 is superimposed for comparison.

For convenience, a definition of the diameter of the focal ring is necessary. For the AAFV beam, the cross-section of the focal plane is a doughnut-shaped focal ring, as shown in Fig. 5(a). The line profile of the intensity distribution along the red dashed line is shown with blue line in Fig. 5(b). The middle black dashed line indicates the position at which the intensity falls to half of the maximum intensity. Meanwhile, this line intersects the intensity line profile at four points. Here, the distance between the inner two points (shown with the red double arrow) is defined as the inner diameter of AAFV beam.
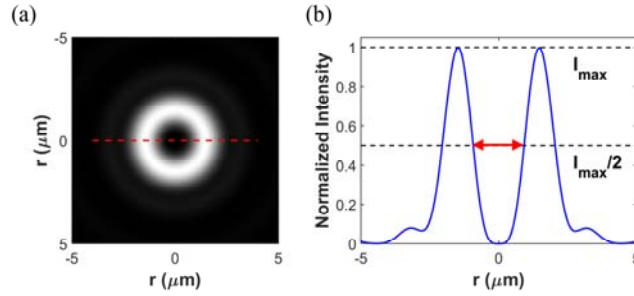

Fig. 5. (a) The cross-section of the focal plane. (b) The corresponding intensity distribution along the red dashed line of (a).

Table 1. Focusing properties for the AAFV beams of the fixed topological charge ($l = 2$)

Degree of polynomial	Axial Positions (μm)			Inner diameters (μm)		
	$n = 2$	$n = 3$	$n = 4$	$n = 2$	$n = 3$	$n = 4$
Analytical results	28.9	31.2	30.4	1.78	1.93	1.87
Numerical simulation	29.1	31.2	30	1.71	1.94	1.90
Experimental results	28.8	31.5	30.6	1.68	1.87	1.93

For the AAFV beams of a fixed topological charge ($l = 2$) with different degrees of polynomials ($n = 2, 3, 4$), the axial positions as well as the focal ring sizes are summarized in Table 1. The analytical results are calculated from the caustic in Eq. (7) and Eq. (4). The minor

discrepancies among the numerical simulation, experimental and analytical results are attributed to the imperfect Gaussian distribution of the input beam. Except these minor mismatches, these results are consistent with each other. This also demonstrates the validity of our analytical results.
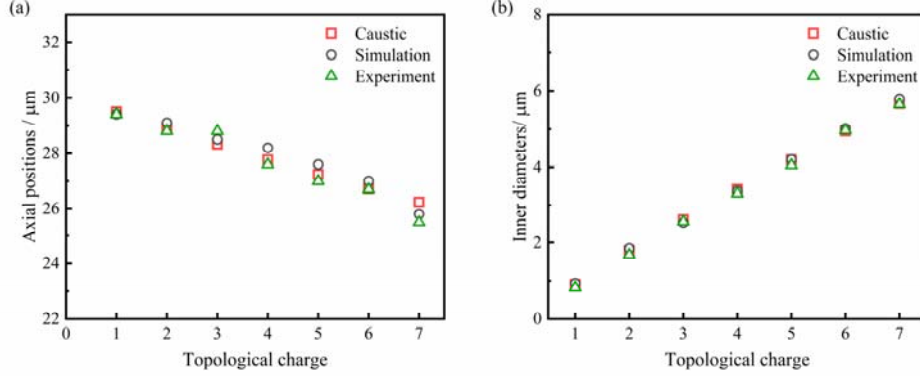

Fig. 6. (a) The axial positions and (b) the inner diameters of focal rings with a fixed degree of polynomial $n = 2$ and variable topological charges from $l = 1$ to $l = 7$.

We further studied the focusing properties of AAFV beams of a fixed degree of polynomial ($n = 2$) with variable topological charges ranging from $l = 1$ to $l = 7$. The variations of the axial positions and the inner diameters of the focal rings are shown in Fig. 6, and the analytical values of the above parameters present less than ~4% differences from the simulations of the ideal case. The numerical simulation, experimental and analytical results from caustics are still consistent with each other. It is obvious that the axial positions of the focal rings are shifted forward as the topological charge increases. Besides, the inner diameters of the focal rings also increase at the same time.

4.2 Manipulation of the focal ring of AAFV beams with a scaling factor

As mentioned above, the axial positions and the inner diameters of the focal rings can be obtained from the analytical caustics. For particle trapping and micromachining applications, it is very useful to facilitate the beam manipulation. Here, we introduce a scaling factor s to scale the global structure and the focusing properties of the AAFV beams. In our scheme, the total phase and the component of the k-vector can be expressed as

$$\phi(r,\theta,s) = -sk\frac{n^2}{(2n-1)(n-1)}\left[(n-1)a\right]^{\frac{1}{n}}(r-r_0)^{\frac{2n-1}{n}} + l\theta \quad n = 2,3,4,\ldots$$

$$k_r(s) = \frac{\partial\phi(r,\theta,s)}{\partial r} = sk_r, \quad k_\theta(s) = k_\theta$$
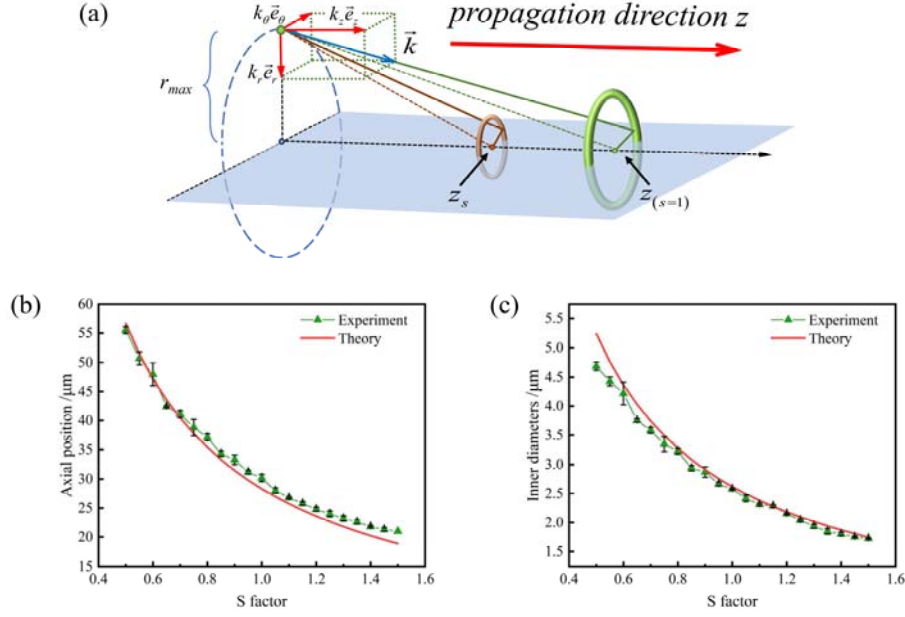
(9)

Fig. 7. (a) The geometrical schematic with a scaling factor s. For a given benchmark AAFV beam, the continuum of rays emerging from the left most ring (blue dashed circle) with a radius r_{max} in the plane $z = 0$ first form the hyperboloids defining the benchmark focal ring (green) in the plane z ($s = 1$). After introducing a scaling factor s, the scaled focal ring (brown) axially shifts in the plane $z = z_s$. The dependence of (b) the axial positions and (c) the inner diameters of focal rings, extracted from the experimental results and our theory with $l = 3$, $n = 2$, on different scaling factor s.

Since the rays from the outmost circle in the plane z = 0 contribute most to the focal ring, we plot the geometrical schematic of the scaled ($s \neq 1$) and the benchmark focal rings ($s = 1$) in Fig. 6(a). Noting that the scaling factor s only affects the k_r and k_z components of the k-vector. After the mathematical calculation, the scaled axial positions z_s and the inner diameters r_s of the focal rings can be written as

$$z_s = \frac{1}{s}\sqrt{z_{(s=1)}^2 + r_{max}^2\left(1 - s^2\right)}$$

$$r_s = \frac{1}{s}r_{(s=1)} \tag{10}$$

Actually, the dependence of z_s on s can be simplified as $z_s \sim z_{(s=1)}/s$ in the paraxial approximation. As an example, we generate the AAFV beam with $n = 2$, $l = 3$ and tweak the scaling factor s from 0.5 to 1.5. The axial positions and the inner diameters of the focal rings calculated from Eq. (10) as well as the experimental results are shown in Fig. 7(b) and 7(c). The experimental results are obtained by taking the average from three repeated measurements on each data point. The discrepancies between the experimental results and our theoretical predictions are less than 1.9 μm and 0.5 μm for axial positions and inner diameters, respectively. The slight differences are attributed to the imperfect Gaussian distribution of the input beam.

4. Conclusion

In this paper, we analyze the caustic of the AAFV beams generated from the polynomial phase mask of the AAF beams with optical vortices. For a given set of the degree of the polynomial n and topological charge l, the families of straight rays emerging from different concentric

circles in the initial plane are winding on different hyperboloids which are overlapped with each other. With the ray-based methods, we also obtain the analytical envelope of the family of the above hyperboloids, *i.e.* the global caustic of the AAFV beam. Our analytical results can well predict the global caustic trajectory of the AAFV beams, especially the physical trajectory deviating from the predefined polynomials. Besides, the axial positions and the inner diameters of the focal rings can also be determined from our analytical formulae. Based on the above analytical results, we further demonstrate our manipulation scheme to tweak the axial positions and the inner diameters of the focal rings with a scaling factor *s*. All of our theoretical results are in excellent agreement with both the numerical simulations and the experimental results. We expect that our results will be beneficial to numerous applications requiring determined beam size and higher intensity, such as particle micromanipulation and material processing.

Disclosures. The authors declare no conflicts of interest.

References

1. N. K. Efremidis and D. N. Christodoulides, "Abruptly autofocusing waves," Opt. Lett. **35**(23), 4045–4047 (2010).
2. D. G. Papazoglou, N. K. Efremidis, D. N. Christodoulides, and S. Tzortzakis, "Observation of abruptly autofocusing waves," Opt. Lett. **36**(10), 1842–1844 (2011).
3. Chremmos, P. Zhang, J. Prakash, N. K. Efremidis, D. N. Christodoulides, and Z. Chen, "Fourier-space generation of abruptly autofocusing beams and optical bottle beams," Opt. Lett. **36**(18), 3675–3677 (2011).
4. I. Chremmos, N. K. Efremidis, and D. N. Christodoulides, "Pre-engineered abruptly autofocusing beams," Opt. Lett. **36**(10), 1890–1892 (2011).
5. J. A. Davis, D. M. Cottrell, and J. M. Zinn, "Direct generation of abruptly focusing vortex beams using a 3/2 radial phase-only pattern," Appl. Opt. **52**(9), 1888–1891 (2013).
6. E. Greenfield, M. Segev, W. Walasik, and O. Raz, "Accelerating light beams along arbitrary convex trajectories," Phys. Rev. Lett. **106**(21), 213902 (2011).
7. L. Froehly, F. Courvoisier, A. Mathis, M. Jacquot, L. Furfaro, R. Giust, P. A. Lacourt, and J. M. Dudley, "Arbitrary accelerating micron-scale caustic beams in two and three dimensions," Opt. Express **19**(17), 16455-16465 (2011).
8. I. D. Chremmos, Z. Chen, D. N. Christodoulides, and N. K. Efremidis, "Abruptly autofocusing and autodefocusing optical beams with arbitrary caustics," Phys. Rev. A **85**(2), 023828 (2012).
9. Z. Zhao, C. Xie, D. Ni, Y. Zhang, Y. Li, F. Courvoisier, and M. Hu, "Scaling the abruptly autofocusing beams in the direct-space," Opt. Express **25**(24), 30598–30605 (2017).
10. P. Zhang, J. Prakash, Z. Zhang, M. S. Mills, N. K. Efremidis, D. N. Christodoulides, and Z. Chen, "Trapping and guiding microparticles with morphing autofocusing Airy beams," Opt. Lett. **36**(15), 2883–2885 (2011).
11. Y. Jiang, K. Huang, and X. Lu, "Radiation force of abruptly autofocusing Airy beams on a Rayleigh particle," Opt. Express **21**(20), 24413–24421 (2013).
12. Y. Jiang, Z. Cao, H. Shao, W. Zheng, B. Zeng, and X. Lu, "Trapping two types of particles by modified circular Airy beams," Opt. Express **24**(16), 18072–18081 (2016).
13. N. K. Efremidis, Z. Chen, M. Segev, and D. N. Christodoulides, "Airy beams and accelerating waves: an overview of recent advances," Optica **6**(5), 686–701 (2019).
14. M. Manousidaki, D. G. Papazoglou, M. Farsari, and S. Tzortzakis, "Abruptly autofocusing beams enable advanced multiscale photo-polymerization," Optica **3**(5), 525–530 (2016).
15. P. Panagiotopoulos, D. G. Papazoglou, A. Couairon, and S. Tzortzakis, "Sharply autofocused ring-Airy beams transforming into non-linear intense light bullets," Nat. Commun. **4**(1), 2622 (2013).
16. J. D. Ring, J. Lindberg, A. Mourka, M. Mazilu, K. Dholakia, and M. R. Dennis, "Auto-focusing and self-healing of Pearcey beams," Opt. Express **20**(17), 18955–18966 (2012).
17. X. Chen, D. Deng, J. Zhuang, X. Peng, D. Li, L. Zhang, F. Zhao, X. Yang, H. Liu, and G. Wang, "Focusing properties of circle Pearcey beams," Opt. Lett. **43**(15), 3626–3629 (2018).
18. S. N. Khonina, A. P. Porfirev, and A. V. Ustinov, "Sudden autofocusing of superlinear chirp beams," J. Opt. **20**(2), 025605 (2018).

19. S. N. Khonina, A. V. Ustinov, and A. P. Porfirev, "Aberration laser beams with autofocusing properties," Appl. Opt. **57**(6), 1410–1416 (2018).
20. L. Allen, M. W. Beijersbergen, R. J. C. Spreeuw, and J. P. Woerdman, "Orbital angular momentum of light and the transformation of Laguerre-Gaussian laser modes," Phys. Rev. A **45**(11), 8185–8189 (1992).
21. A. Wallraff, A. Lukashenko, J. Lisenfeld, A. Kemp, M. V. Fistul, Y. Koval, and A. V. Ustinov, "Quantum dynamics of a single vortex," Nature **425**(6954), 155–158 (2003).
22. Z. Wang, N. Zhang, and X.-C. Yuan, "High-volume optical vortex multiplexing and de-multiplexing for free-space optical communication," Opt. Express **19**(2), 482–492 (2011).
23. Y. Yan, G. Xie, M. P. J. Lavery, H. Huang, N. Ahmed, C. Bao, Y. Ren, Y. Cao, L. Li, Z. Zhao, A. F. Molisch, M. Tur, M. J. Padgett, and A. E. Willner, "High-capacity millimetre-wave communications with orbital angular momentum multiplexing," Nat. Commun. **5**, 4876(2014).
24. D. G. Grier, "A revolution in optical manipulation," Nature **424**(6950), 810–816 (2003).
25. M. Padgett and R. Bowman, "Tweezers with a twist," Nat. Photonics **5**(6), 343–348 (2011).
26. C. Hnatovsky, V. G. Shvedov, W. Krolikowski, and A. V. Rode, "Materials processing with a tightly focused femtosecond laser vortex pulse," Opt. Lett. **35**(20), 3417-3419 (2010).
27. M. K. Sharma, J. Joseph, and P. Senthilkumaran, "Selective edge enhancement using anisotropic vortex filter," Appl. Opt. **50**(27), 5279-5286 (2011).
28. Y. Jiang, K. Huang, and X. Lu, "Propagation dynamics of abruptly autofocusing Airy beams with optical vortices," ~~vortices,"~~ Opt. Express **20**(17), 18579–18584 (2012).
29. Y. Jiang, S. Zhao, W. Yu, and X. Zhu, "Abruptly autofocusing property of circular Airy vortex beams with different initial launch angles," J. Opt. Soc. Am. A **35**(6), 890–894 (2018).
30. J. A. Davis, D. M. Cottrell, and D. Sand, "Abruptly autofocusing vortex beams," Opt. Express **20**(12), 13302–13310 (2012).
31. B. Chen, C. Chen, X. Peng, Y. Peng, M. Zhou, and D. Deng, "Propagation of sharply autofocused ring Airy Gaussian vortex beams," Opt. Express **23**(15), 19288–19298 (2015).
32. M. Chen, S. Huang, W. Shao, and X. Liu, "Experimental study on the propagation characteristics of ring Airy Gaussian vortex beams," Appl. Phys. B **123**(8), 215 (2017).
33. X. Yan, L. Guo, M. Cheng, and S. Chai, "Free-space propagation of autofocusing Airy vortex beams with controllable intensity gradients," Chin. Opt. Lett. **17**(4), 040101 (2019).
34. X Zhang, P Li, S Liu, B Wei, S Qi, X Fan, S Wang, and J Zhao, "Autofocusing of ring Airy beams embedded with off-axial vortex singularities," Opt. Express **28**(6), 7953-7960 (2020).
35. Y. Qian, Y. Shi, W. Jin, F. Hu, and Z. Ren, "Annular arrayed-Airy beams carrying vortex arrays," Opt. Express **27**(13), 18085–18093 (2019).
36. A. Brimis, K. G. Makris, and D. G. Papazoglou, "Tornado waves," Opt. Lett. **45**(2), 280–283 (2020).
37. S. N. Khonina, A. P. Porfirev, A. V. Ustinov, and M. A. Butt, "Generation of complex transverse energy flow distributions with autofocusing optical vortex beams," Micromachines **12**(3), 297-(12p) (2021).
38. V. A. Soifer, S. I. Kharitonov, S. N. Khonina, and S. G. Volotovsky, "Caustics of vortex optical beams," Dokl. Phys. **64**, 276–279 (2019).
39. S. I. Kharitonov, S. N. Khonina, S. G. Volotovsky, and N. L. Kazanskiy, "Caustics of the vortex beams generated by vortex lenses and vortex axicons," JOSA A **37** (3), 476-482 (2020).
40. Y. A. Kravtsov and Y. I. Orlov, "Geometrical Optics of Inhomogeneous Media," Springer Berlin (1990).
41. Y. A. Kravtsov and Y. I. Orlov, "Caustics, Catastrophes and Wave Fields," Springer Berlin, 2nd Edition (1999).
42. M. V. Berry and K. T. McDonald, "Exact and geometrical optics energy trajectories in twisted beams," J. Opt. A, Pure Appl. Opt. **10**(3), 035005 (2008).
43. M. A. Alonso and G. Forbes, "Stable aggregates of flexible elements give a stronger link between rays and waves," Opt. Express **10**(16), 728–739 (2002).
44. G.W. Forbes and M.A. Alonso, "Using rays better. I. Theory for smoothly varying media," J. Opt. Soc. Am. A **18**(5), 1132–1145 (2001).
45. C. Xie, R. Giust, V. Jukna, L. Furfaro, M. Jacquot, P. A. Lacourt, L. Froehly, J. Dudley, A. Couairon, and F. Courvoisier, "Light trajectory in Bessel–Gauss vortex beams," J. Opt. Soc. Am. A **32**(7), 1313-1316 (2015).
46. I. N. Bronshtein and K. A. Semendyayev, "A guide book to Mathematics," Springer New York (1973).
47. J. W. Goodman, "Introduction to Fourier Optics," McGraw-Hill, 2nd Ed (1996).